Solid State Ionics 325 (2018) 102–111

Contents lists available at ScienceDirect

Solid State Ionics

journal homepage: www.elsevier.com/locate/ssi

Ab initio based interionic potential for silver iodide

Hongwei Niu[a], Yuhang Jing[a,b,c,*], Yi Sun[a,**], Narayana R. Aluru[c]

[a] Department of Astronautical Science and Mechanics, Harbin Institute of Technology, Harbin, Heilongjiang 150001, PR China
[b] National Center for Supercomputing Applications (NCSA), University of Illinois at Urbana–Champaign, Urbana, IL 61801, USA
[c] Department of Mechanical Science and Engineering, Beckman Institute for Advanced Science and Technology, University of Illinois at Urbana–Champaign, Urbana, IL 61801, USA

ARTICLE INFO

Keywords:
Silver iodide
Lattice inversion
Density functional theory
Molecular dynamics simulation

ABSTRACT

In this paper, a new interionic potential is derived for silver iodide (AgI) *via* the Chen-Möbius lattice inversion and *ab initio* calculation. The accuracy of the proposed potential is checked by comparing the molecular dynamics simulation results on the static properties, structural stability, disordered states, mean-squared displacement and phase transition of AgI with experimental data. The simulation results are consistent with experimental data and density functional theory (DFT) calculations, indicating that the proposed interionic potential is valid over a wide range of interionic separations and applicable for describing the major properties of AgI.

1. Introduction

Superionic conductors have attracted much attention because of their potential for applications in solid electrolytes [1–3], fast-response gas sensors [4,5], and photographic materials [6–9]. Among various superionic compounds, silver iodide (AgI) is well known due to its high ionic conductivity and stability. The ionic and electrical conductivities of AgI have been measured experimentally [10–15]. α-AgI, the high-temperature phase of AgI, displays a high ionic conductivity with weak dependence on temperature from 147 °C to 555 °C. However, the highly ionic conducting α-AgI undergoes a phase transition into a normal ionic conducting β-AgI at 147 °C. In the low temperature β phase, the iodine ions form a hcp lattice while the silver ions are tetrahedrally bonded to each iodine and exhibit no self-diffusion. In the high temperature α phase, the iodine ions form a bcc lattice and exhibit self-diffusion and high mobility. X-ray [16–18], neutron diffraction [19–21], and extended X-ray absorption fine structure [22–24] measurements are performed to determine the structure of AgI. To understand the mechanism of this phase transition, many correlative investigations from both experiments and theoretical calculations have been performed [25–27]. However, in order to obtain a deeper understanding of the nature of ionic motions and the phase transition, atomistic scale simulations are needed to provide the necessary microscopic perspective [28]. Density functional theory (DFT) calculations are typically used to study the static properties of small systems. Alternatively, molecular dynamics (MD) simulations have been widely used to study the dynamic properties of larger systems. The structure factor of AgI, the diffusion constant of Ag^+ and its temperature dependence are obtained from MD simulations and the results are consistent with experimental data [29–34]. However, reproducing the phase transition is still a challenging task for MD simulations and the accuracy of MD simulations directly depends on the accuracy of the potentials used. Although the $\alpha \rightleftharpoons \beta$ phase transition of AgI is observed in MD simulations based on the potential developed by Rahman, Vashishta and Parrinello [32] (known as RVP potential), a robust potential which can capture both static (*e.g.*, lattice constants, cohesive energy, and elastic constants) and dynamic (*e.g.*, phase transition and ionic diffusion constant) characteristics of AgI is needed, which is currently missing. Recently, the lattice inversion (LI) method proposed by Chen [35] has been successfully applied to derive the short-range pairwise potential for alkali halides, solid oxides, metal alloys, and semiconductors [36–40]. On the basis of the information on the interatomic interactions from *ab initio* calculations, the potential form can be determined and its parameters can be evaluated. Therefore, the potentials derived by the LI method inherit the accuracy from *ab initio* calculations.

In the current work, the LI technique is employed to derive the interionic potential for AgI. The idea is to first construct several extended structures of AgI and perform the *ab initio* cohesive energy calculations. Then the short-range interactions are directly derived from a series of cohesive energy differences using the LI method. Next, the functional

* Correspondence to: Y. Jing, Department of Astronautical Science and Mechanics, Harbin Institute of Technology, Harbin, Heilongjiang 150001, PR China.
** Corresponding author.
E-mail addresses: yhjing@hit.edu.cn (Y. Jing), sunyi@hit.edu.cn (Y. Sun).

https://doi.org/10.1016/j.ssi.2018.07.027
Received 3 May 2018; Received in revised form 23 July 2018; Accepted 30 July 2018
Available online 18 August 2018
0167-2738/

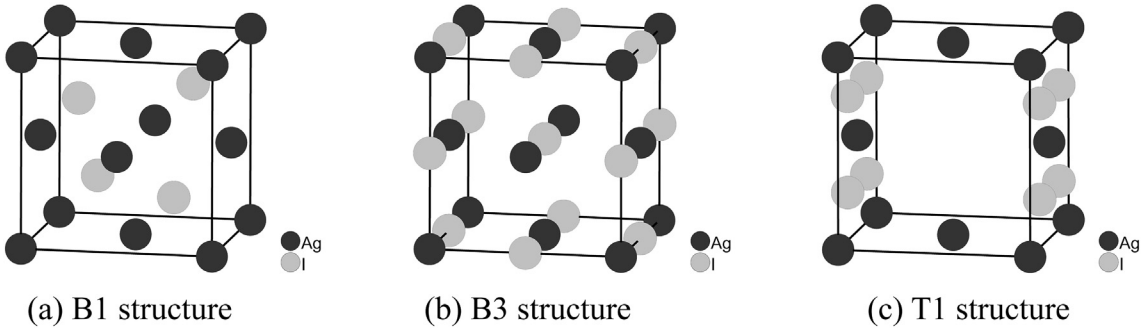

Fig. 1. Extended AgI structures used for the *ab initio* cohesive energy calculations.

form and its initial parameters are evaluated by fitting the inverted potential. Finally, the parameters are optimized with the training set from *ab initio* calculations. Furthermore, on the basis of the proposed potential, several applications are given for verification purpose. Static properties, structural stability, disordered states, mean-squared displacement and phase transition of AgI are discussed in detail.

2. Derivation of interionic potential of AgI

For the AgI system, the cohesive energy can be expressed as

$$E_{coh} = E_{cou} + E_{Ag\text{-}I(SR)} + E_{I\text{-}I(SR)} + E_{Ag\text{-}Ag(SR)}, \quad (1)$$

where E_{cou} is the long-range part (Coulomb energy) and E_{SR} is the short-range part. The long-range part is evaluated using the Ewald summation technique [41], while the short-range part is derived from an extended phase space including several virtual structures as shown in Fig. 1.

In this paper, the cohesive energies of B1-, B3- and T1-AgI are calculated by DFT with the Vienna *Ab initio* Simulation Package (VASP) [42–44]. The Perdew-Burke-Ernzerhof (PBE) [45] exchange-correlation functional is utilized based on the projector augmented wave (PAW) method [44]. The unit cells are optimized using a 12 × 12 × 12 Monkhorst-Pack k-points mesh and the cutoff energy for the plane wave basis set is 500 eV. The pseudopotentials with valence states of Ag (4s, 4p, 5s, 4d) and I (5s, 5p) are employed for more accuracy. All ionic positions are optimized with the conjugate gradient algorithm until the forces on each ion are < 0.01 eV/Å. All the calculations are spin polarized. Fig. 2 depicts the calculated cohesive energies of the three extended phases as a function of the lattice constant.

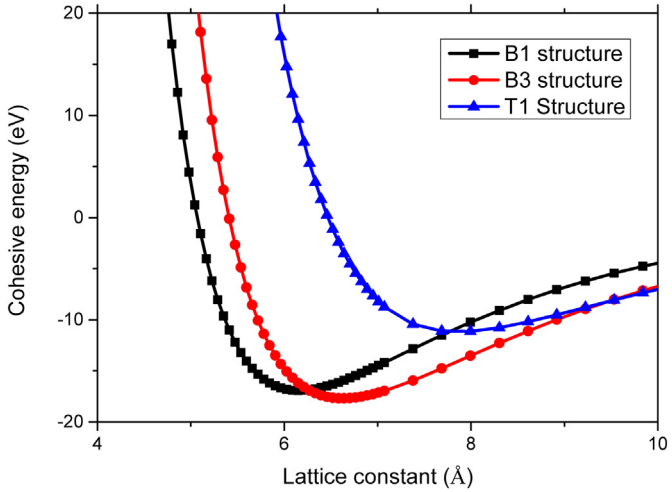

Fig. 2. Cohesive energies *versus* lattice constant in B1-, B3- and T1-AgI structures from the *ab initio* calculations.

2.1. Ag-I interionic potential

The cohesive energy $E_{coh}{}^{B1}(a)$ of B1-type AgI for a lattice constant a can be written as in Eq. (2), which includes three kinds of ionic interactions, $E_{Ag\text{-}Ag}{}^{fcc}(a)$, $E_{I\text{-}I}{}^{fcc}(a)$, and $E_{AgI}{}^{B1}(a)$,

$$E_{coh}^{B1}(a) = E_{Ag\text{-}Ag}^{fcc}(a) + E_{I\text{-}I}^{fcc}(a) + E_{Ag\text{-}I}^{B1}(a), \quad (2)$$

where $E_{Ag\text{-}Ag}{}^{fcc}(a)$ and $E_{I\text{-}I}{}^{fcc}(a)$ are the contributions of uniform ions on the fcc (face-centered-cubic) sublattice, and $E_{Ag\text{-}I}{}^{B1}(a)$ is the contribution of unlike ions.

Similarly, the cohesive energy $E_{coh}{}^{B3}(a)$ of B3-type AgI for a lattice constant a can be written as Eq. (3).

$$E_{coh}^{B3}(a) = E_{Ag\text{-}Ag}^{fcc}(a) + E_{I\text{-}I}^{fcc}(a) + E_{I\text{-}I}^{B3}(a). \quad (3)$$

The cohesive energy combines both short-range and long-range interactions. Using Eqs. (2) and (3), the short-range Ag-I interaction difference between B1- and B3-AgI can be written as

$$\begin{aligned}\Delta E_{Ag\text{-}I(SR)}(a) &= E_{Ag\text{-}I(SR)}^{B3}(a) - E_{Ag\text{-}I(SR)}^{B1}(a)\\ &= (E_{Ag\text{-}I(coh)}^{B3}(a) - E_{Ag\text{-}I(cou)}^{B3}(a)) - (E_{Ag\text{-}I(coh)}^{B1}(a) - E_{Ag\text{-}I(cou)}^{B1}(a)),\\ &= (E_{coh}^{B3}(a) - E_{cou}^{B3}(a)) - (E_{coh}^{B1}(a) - E_{cou}^{B1}(a))\end{aligned} \quad (4)$$

where $E_{coh}{}^{B3}(a)$ and $E_{coh}{}^{B1}(a)$ are determined from the *ab initio* calculation as shown in Fig. 2. $E_{cou}{}^{B3}(a)$ and $E_{cou}{}^{B1}(a)$ are evaluated by the Ewald summation technique with the value of charge, $+0.6e$ for Ag^+ and $-0.6e$ for I^-, which is kept the same as in the RVP potential.

Based on Eq. (4), the short-range Ag-I interaction difference between B1- and B3-AgI is obtained as shown in Fig. 3(a).

For the mixed virtual lattice B3-B1, the relation between the cohesive energy difference $\Delta E_{Ag\text{-}I(SR)}(a)$ and the interionic potential $\phi_{Ag\text{-}I}$ is given by

$$\begin{aligned}\Delta E_{Ag\text{-}I(SR)}(a) &= E_{Ag\text{-}I(SR)}^{B3}(a) - E_{Ag\text{-}I(SR)}^{B1}(a)\\ &= \frac{1}{2}\sum_{i,j,k}\phi_{Ag\text{-}I}^{SR}\left(\sqrt{(i+k-1/2)^2+(i+j-1/2)^2+(i+k-1/2)^2}\,\frac{a}{2}\right).\\ &- \frac{1}{2}\sum_{i,j,k}\phi_{Ag\text{-}I}^{SR}\left(\sqrt{(i+k-1)^2+(i+j-1)^2+(i+k-1)^2}\,\frac{a}{2}\right)\end{aligned} \quad (5)$$

From Eq. (5), the short-range Ag-I pair potential curve can be derived directly by Chen-Möbius LI techniques, as shown in Fig. 3(b). Morse function [46] is used to fit the curve. Combining both the short-range term and the Coulomb term, the total Ag-I pair potential is given by

$$\phi_{Ag\text{-}I} = D_{+-}(e^{-2\alpha_{+-}(r-R_{+-})} - 2e^{-\alpha_{+-}(r-R_{+-})}) + \frac{q_+q_-}{4\pi\varepsilon_0 r}, \quad (6)$$

where D_{+-}, α_{+-} and R_{+-} are the parameters of the Morse potential between cation and anion.

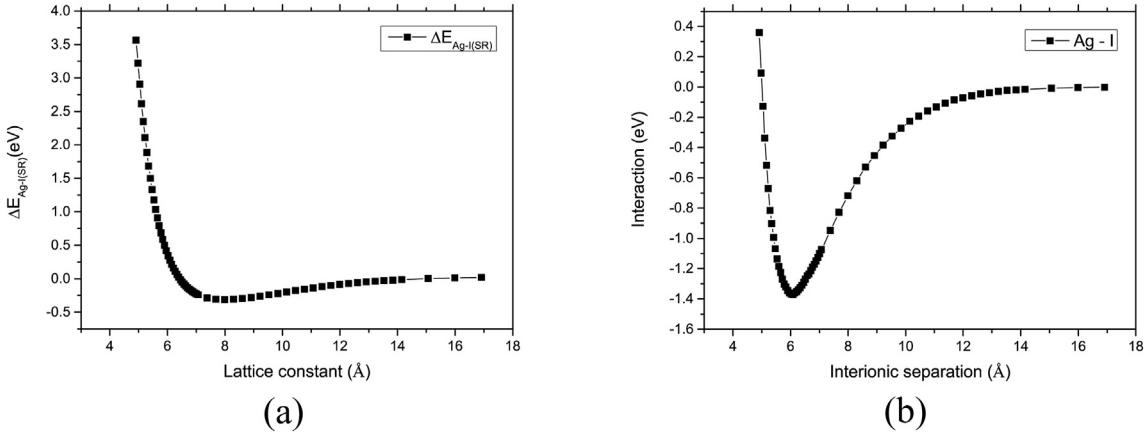

Fig. 3. (a) The short-range Ag-I interaction difference between B1- and B3-AgI *versus* lattice constant and (b) the short-range Ag-I pair potential *versus* interionic separation, which is derived from panel (a).

2.2. I-I interionic potential

The cohesive energy $E_{coh}^{T1}(a)$ of T1-type AgI for a lattice constant a can be written as,

$$E_{coh}^{T1}(a) = E_{Ag\text{-}Ag}^{fcc}(a) + E_{I\text{-}I}^{tetra}(a) + E_{Ag\text{-}I}^{T1}(a). \tag{7}$$

Using Eqs. (2) and (7), the short-range I-I interaction difference between B1- and T1-AgI can be expressed as

$$\begin{aligned}\Delta E_{I\text{-}I(SR)}(a) &= E_{I\text{-}I(SR)}^{B1}(a) - E_{I\text{-}I(SR)}^{T1}(a)\\ &= (E_{I\text{-}I(coh)}^{B1}(a) - E_{I\text{-}I(cou)}^{B1}(a)) - (E_{I\text{-}I(coh)}^{T1}(a) - E_{I\text{-}I(cou)}^{T1}(a)),\\ &= (E_{coh}^{B1}(a) - E_{cou}^{B1}(a) - E_{Ag\text{-}I(SR)}^{B1}(a)) - (E_{coh}^{T1}(a) - E_{cou}^{T1}(a) - E_{Ag\text{-}I(SR)}^{T1}(a))\end{aligned} \tag{8}$$

where $E_{coh}^{B1}(a)$ and $E_{coh}^{T1}(a)$ are determined from *ab initio* calculation as shown in Fig. 2, $E_{Ag\text{-}I(SR)}^{B1}(a)$ and $E_{Ag\text{-}I(SR)}^{T1}(a)$ are derived using the inverted Ag-I pair potential given in Eq. (6).

Based on Eq. (8), the short-range I-I interaction difference between B1- and T1-AgI is obtained as shown in Fig. 4(a).

For the mixed virtual lattice B1-T1, the relation between the cohesive energy $\Delta E_{I\text{-}I(SR)}(a)$ and the interionic potential $\phi_{I\text{-}I}$ is given by,

$$\begin{aligned}\Delta E_{I\text{-}I(SR)}(a) &= E_{I\text{-}I(SR)}^{B1}(a) - E_{I\text{-}I(SR)}^{T1}(a)\\ &= \frac{1}{2}\sum_{i,j,k}\phi_{I\text{-}I}^{SR}\left(\sqrt{(i+k)^2+(i+j)^2+(j+k)^2}\,\frac{a}{2}\right).\\ &- \frac{1}{2}\sum_{i,j,k}\phi_{I\text{-}I}^{SR}\left(\sqrt{i^2+4j^2+k^2}\,\frac{a}{2}\right)\end{aligned} \tag{9}$$

Similarly, from Eq. (9), the short-range I-I pair potential curve can be derived using the Chen-Möbius LI techniques, as shown in Fig. 4(b). Once again, the Morse function is used to fit the curve. Combining both the short-range term and the Coulomb term, the total I-I pair potential is given by

$$\phi_{I\text{-}I} = D_{--}(e^{-2\alpha_{--}(r-R_{--})} - 2e^{-\alpha_{--}(r-R_{--})}) + \frac{q_-q_-}{4\pi\varepsilon_0 r}, \tag{10}$$

where D_{--}, α_{--} and R_{--} are the parameters of the Morse potential describing interaction between anions.

2.3. Ag-Ag interionic potential

The cation-cation short-range interaction is neglected for the sake of simplicity, which has been adopted for the development of empirical potentials for solid materials [36,37]. Thus, the Ag-Ag interactions are computed by the Coulomb potential,

$$\phi_{Ag\text{-}Ag} = \frac{q_+q_+}{4\pi\varepsilon_0 r}. \tag{11}$$

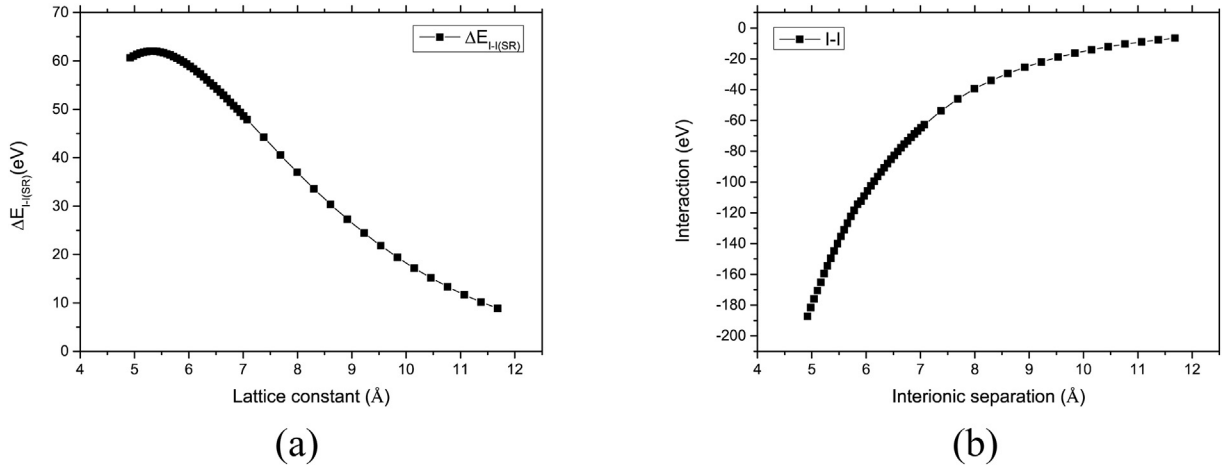

Fig. 4. (a) The short-range I-I interaction difference between B1- and T1-AgI *versus* lattice constant and (b) the short-range I-I pair potential *versus* interionic separation, which is derived from panel (a).

Table 1
The parameters of the proposed potential of AgI.

	D(eV)	α(1/Å)	R(Å)	$q_+ = q_-(e)$
Ag-I	0.5500	1.6000	2.6000	0.3181
I-I	0.1600	0.6840	5.7000	0.3181
Ag-Ag				0.3181

Table 2
Lattice constant a_0, cohesive energy E_{coh}, and elastic constants C_{11}, C_{12} and C_{44} of fcc AgI at zero temperature and pressure.

	a_0(Å)	E_{coh}(eV)	C_{11}(GPa)	C_{12}(GPa)	C_{44}(GPa)
This work	6.25	−4.23	30.64	27.10	27.10
RVP	6.11	−3.69	23.32	15.60	15.60
DFT	6.16	−4.23	49.84	27.24	9.94
Experiment	6.082 [47]				

Table 3
Lattice constant a_0, cohesive energy E_{coh}, and elastic constants C_{11}, C_{12} and C_{44} of γ-AgI at zero temperature and pressure.

	a_0(Å)	E_{coh}(eV)	C_{11}(GPa)	C_{12}(GPa)	C_{44}(GPa)
This work	6.48	−4.40	35.14	24.72	24.72
RVP	6.43	−3.74	19.11	14.08	14.08
DFT	6.63	−4.42	30.36	24.04	9.34
Experiment	6.499 [47]		26.2 [48]	22.9 [48]	8.17 [48]

Table 4
Lattice constant a_0, cohesive energy E_{coh} of β-AgI at zero temperature and pressure.

	a_0(Å)	E_{coh}(eV)
This work	4.58	−4.41
RVP	4.55	−3.74
DFT	4.68	−4.42
Experiment	4.592 [49]	

It should be noted that the strong covalent nature of bonds in AgI could introduce cohesive energy mismatch between the inverted potential and *ab initio* calculation. Optimization is thus performed to minimize the cohesive energy mismatch by adjusting the pair potential parameters, in which *ab initio* calculations in Fig. 2 are treated as the training sets for the genetic algorithms. The modified parameters are tabulated in Table 1.

3. Application of the interionic potential

3.1. Static properties of AgI crystal

We use the interionic potential to compute the static properties of equilibrium fcc, β-, and γ-AgI at zero temperature and pressure. These properties are shown in Tables 2, 3, and 4.

For comparison purposes, these static properties are also computed using DFT and the RVP potential. These calculated values and experimental data are also listed in Tables 2, 3, and 4.

The results in Tables 2, 3 and 4 reveal that the results based on the new potential (this work) are closer to experimental and DFT data than those obtained from the RVP potential. The elastic constants C_{11} and C_{12} based on the present potential are closer to experimental and DFT data in fcc and γ-AgI. C_{44} deviates from experimental and DFT data because of the built-in Cauchy relation, $C_{12} = C_{44}$, in pairwise potential cubic system [50]. In summary, the present potential yields consistent static properties of AgI in fcc, β, and γ phases compared with experimental and DFT data. It has advantages over the RVP potential in describing static properties.

3.2. Stability of AgI crystal

In the present work, structural stability is considered as an important check for the proposed potential. For an effective potential, the interionic forces should enable accurate transitions between deformed structures and equilibrium phases, and between disordered and ordered states. The conjugate gradient algorithm is used for energy minimization. Detailed results are given below.

First, the deformed structures are constructed by varying the lattice parameters, for example, the lattice constant a is varied from $0.75a_0$ to $1.5a_0$ (a_0 is the equilibrium lattice constant) and the axial angles are kept the same or reduced by one third. In some cases, the lattice constants and the axial angles are varied simultaneously. For the ten cases listed in Table 5, their energy minimization is carried out to search for

Table 5
Energy minimization results for the initial deformed configuration to the final stable structure based on different interionic potentials. The lattice parameters are in the units of their equilibrium values a_0, b_0, c_0, α_0, β_0, and γ_0.

Initial (unrelaxed)							Interionic potential	Final (relaxed)					
Phase	a/a_0	b/b_0	c/c_0	α/α_0	β/β_0	γ/γ_0		a/a_0	b/b_0	c/c_0	α/α_0	β/β_0	γ/γ_0
β	1.50	1.50	1.50	1.00	1.00	1.00	RVP	1.00	1.00	1.00	1.00	1.00	1.00
							This work	1.00	1.00	1.00	1.00	1.00	1.00
β	0.75	0.75	0.75	1.00	1.00	1.00	RVP	1.00	1.00	1.00	1.00	1.00	1.00
							This work	1.00	1.00	1.00	1.00	1.00	1.00
β	1.00	1.00	1.00	0.66	0.66	0.66	RVP	1.00	1.00	1.00	1.00	1.00	1.00
							This work	1.00	1.00	1.00	1.00	1.00	1.00
β	1.50	1.50	1.50	0.66	0.66	0.66	RVP	1.00	1.00	1.00	1.00	1.00	1.00
							This work	1.00	1.00	1.00	1.00	1.00	1.00
β	0.75	0.75	0.75	0.66	0.66	0.66	RVP	1.00	1.00	1.00	1.00	1.00	1.00
							This work	1.00	1.00	1.00	1.00	1.00	1.00
γ	1.50	1.50	1.50	1.00	1.00	1.00	RVP	1.00	1.00	1.00	1.00	1.00	1.00
							This work	1.00	1.00	1.00	1.00	1.00	1.00
γ	0.75	0.75	0.75	1.00	1.00	1.00	RVP	1.00	1.00	1.00	1.00	1.00	1.00
							This work	1.00	1.00	1.00	1.00	1.00	1.00
γ	1.00	1.00	1.00	0.66	0.66	0.66	RVP	1.48	1.48	1.48	0.66	0.66	0.66
							This work	1.00	1.00	1.00	1.00	1.00	1.00
γ	1.50	1.50	1.50	0.66	0.66	0.66	RVP	1.48	1.48	1.48	0.66	0.66	0.66
							This work	1.00	1.00	1.00	1.00	1.00	1.00
γ	0.75	0.75	0.75	0.66	0.66	0.66	RVP	1.48	1.48	1.48	0.66	0.66	0.66
							This work	1.00	1.00	1.00	1.00	1.00	1.00

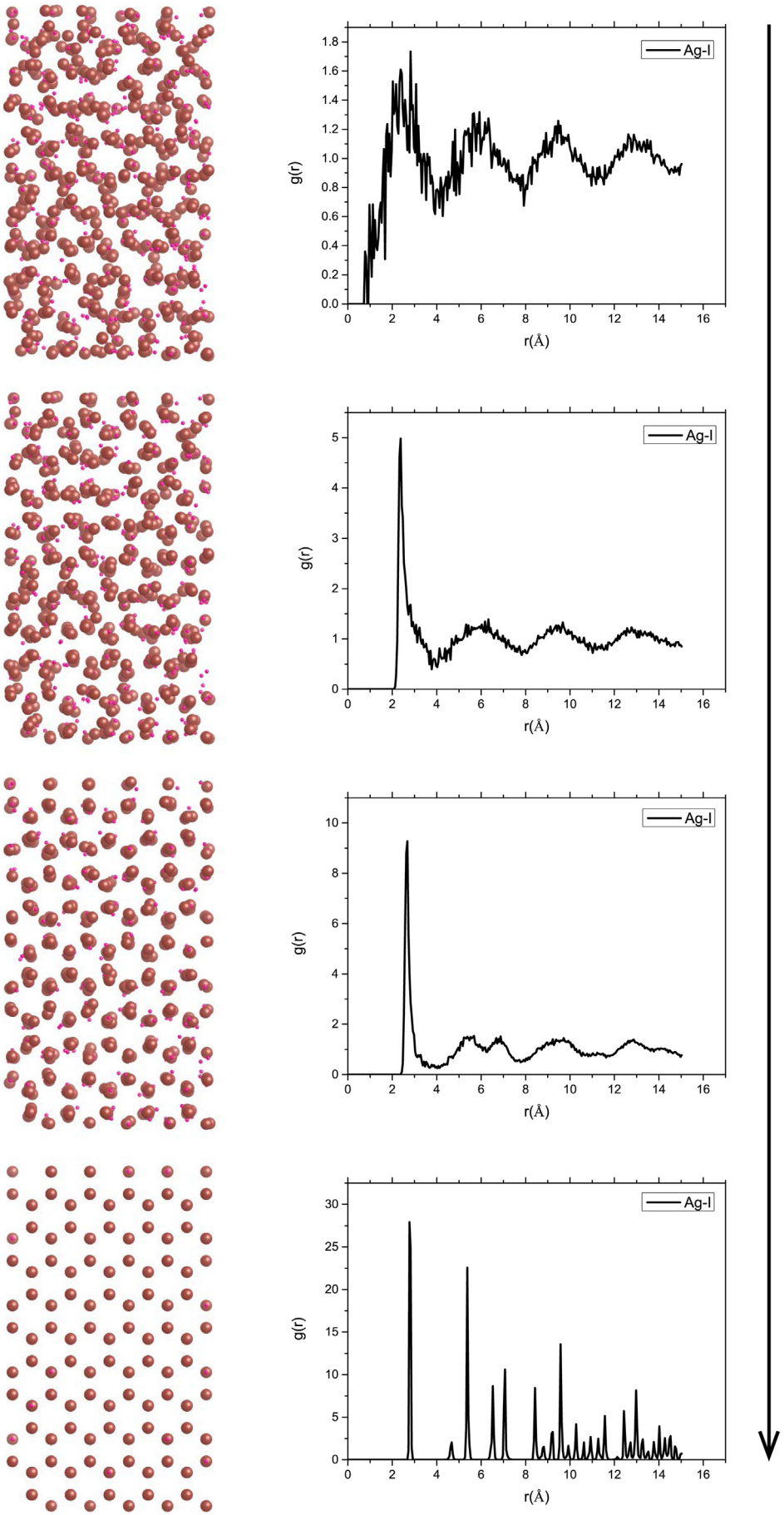

Fig. 5. Snapshots of the configurations during the transition from disordered to ordered β-AgI. The corresponding RDF is also shown.

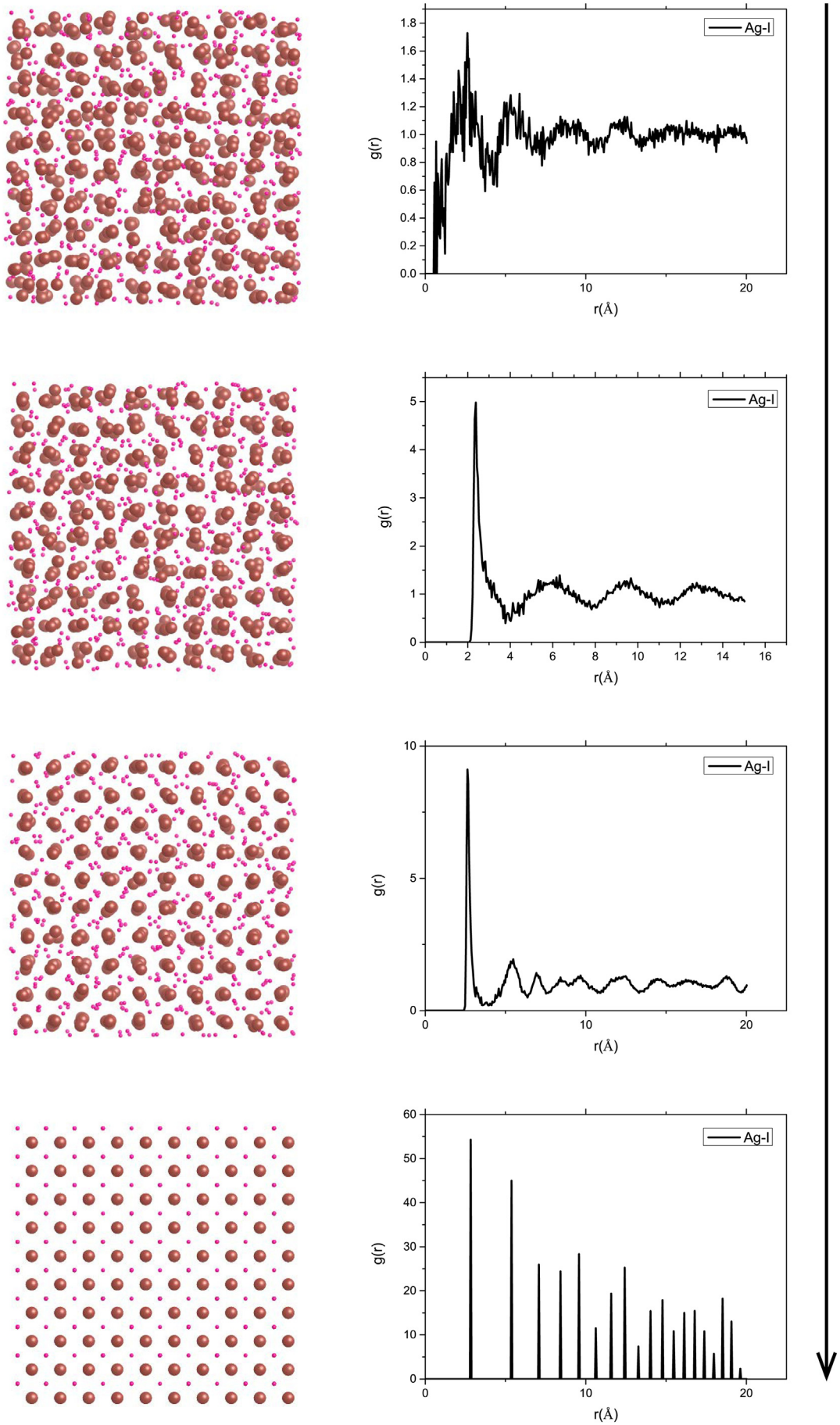

Fig. 6. Snapshots of the configurations during the transition from disordered to ordered γ-AgI. The corresponding RDF is also shown.

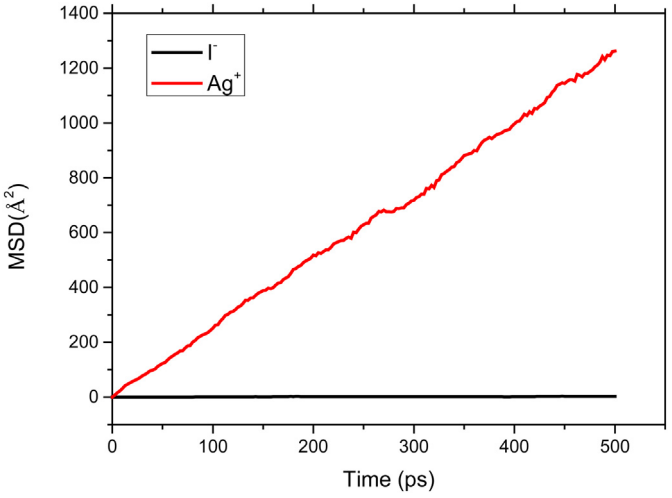

Fig. 7. Mean-squared displacement of Ag^+ and I^- in α-AgI at 773.15 K.

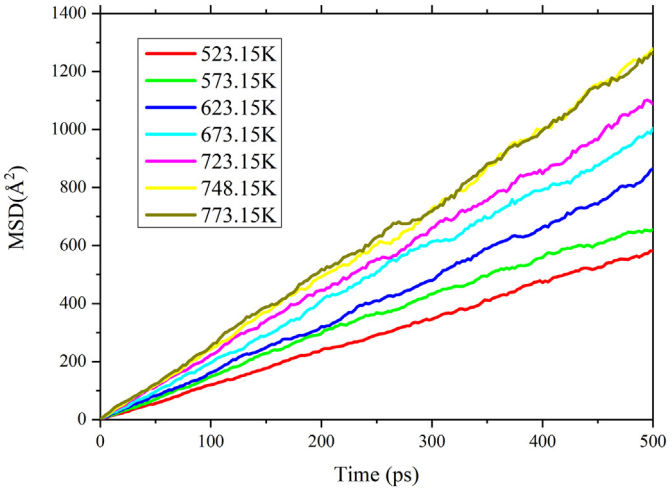

Fig. 8. Mean-squared displacement of Ag^+ at different temperatures from 525.15 K to 773.15 K.

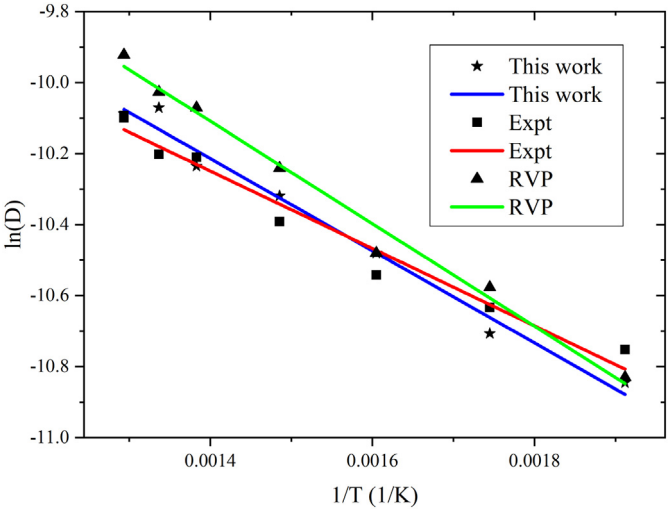

Fig. 9. The natural logarithm of Ag^+ diffusion coefficient (the symbol) *versus* the reciprocal of temperature: Arrhenius curve.

Table 6
The activation energy for diffusion E_A and the pre-exponential factor D_0 for both experimental and simulation data.

	E_A(cal · mol^{-1} · K^{-1})	D_0(cm^2 · s^{-1})
This work	2580	22.57×10^{-5}
RVP	2870	30.77×10^{-5}
Experiment [54]	2190	16.62×10^{-5}

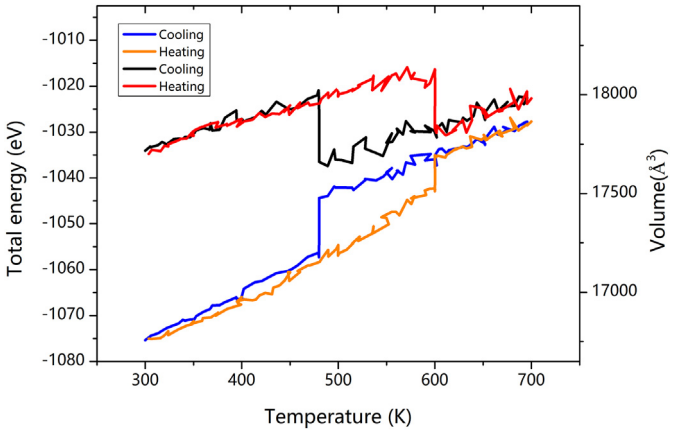

Fig. 10. Temperature dependence of the total energy (blue and orange lines) and volume (black and red lines) of AgI on cooling and heating with the interionic potential developed in this paper. (For interpretation of the references to colour in this figure legend, the reader is referred to the web version of this article.)

the stable configuration given the initial state.

The energy minimization results show that that both RVP and the present potential can characterize the stability of β- and γ-AgI (see Table 5). Three deformed γ-AgI structures, in which the axial angles are reduced, do not return to the equilibrium states based on the RVP potential as these cases might involve calculations that go beyond the validity range of the RVP potential. These tests suggest that the present potential appears to be promising in stabilizing the deformed structures of β- and γ-AgI.

In addition to the deformed structures, the disordered states are constructed by randomly moving all the ions 1.0 Å (36% and 35% of the nearest-neighbor distance of β- and γ-AgI, respectively) from their original sites in periodic supercells with 500 silver ions and 500 iodide ions, as shown in Figs. 5 and 6. Energy minimization drives the disordered structures towards their corresponding ordered state. The snapshots and the radial distribution functions (RDF) of the intermediate configurations are shown in Figs. 5 and 6 to detail the transition process. Both β- and γ-AgI return to their initial states even with a relatively large displacement of 1.0 Å, suggesting that the present potential is valid over a wide range of interionic separation.

3.3. Mean-squared displacement in α-AgI

Mean-squared displacement is defined as

$$\mathrm{MSD}(t) \equiv \langle (\mathbf{r} - \mathbf{r}_0)^2 \rangle = \frac{1}{N} \sum_{n=1}^{N} (\mathbf{r}_n(t) - \mathbf{r}_n(0))^2, \tag{12}$$

where N is the number of ions, $\mathbf{r}_n$ is the position vector of ion n and $\diamond$ denotes time-average.

Using the Einstein-Smoluchowski relation [51,52], the diffusion coefficient D for three-dimensional motion is given by

$$D = \lim_{t \to \infty} \frac{\mathrm{MSD}(t)}{6t}, \tag{13}$$

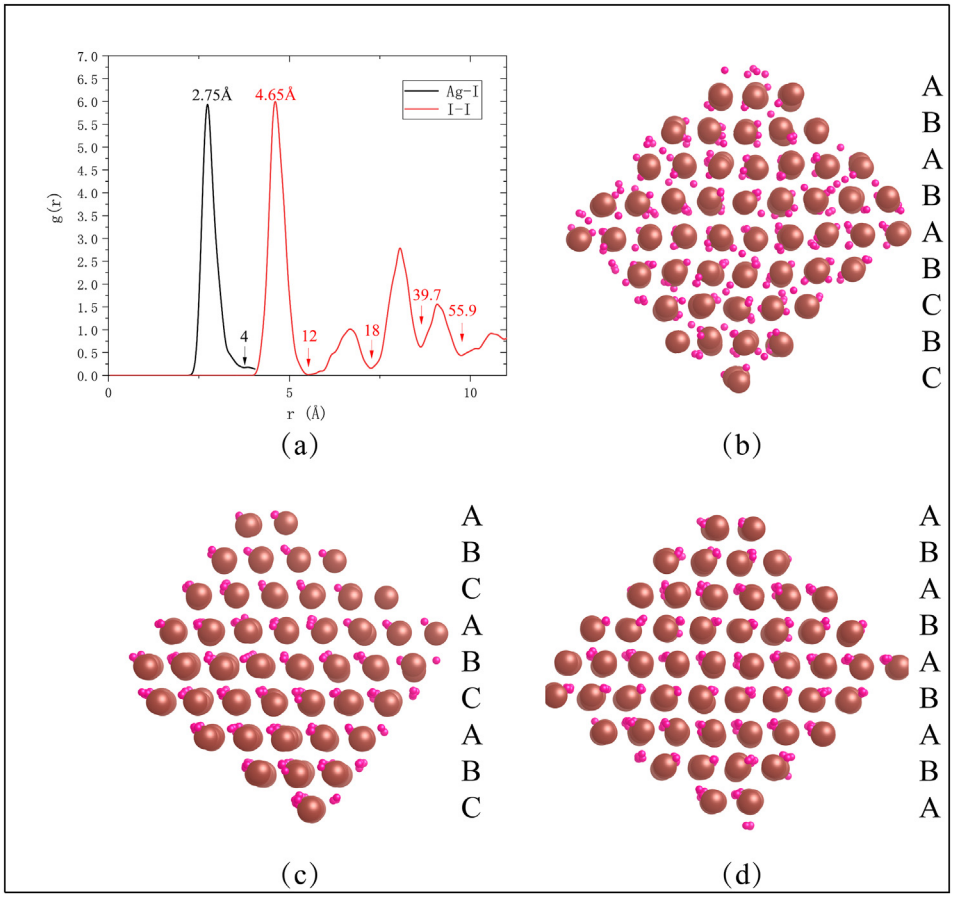

Fig. 11. The RDF (a) and structure (b) at about 480 K after cooling from α-AgI at 700 K. The structures of γ-AgI (c) with fcc iodine sublattice and β-AgI (d) with hcp iodine sublattice at about 480 K is also demonstrated for comparison purposes.

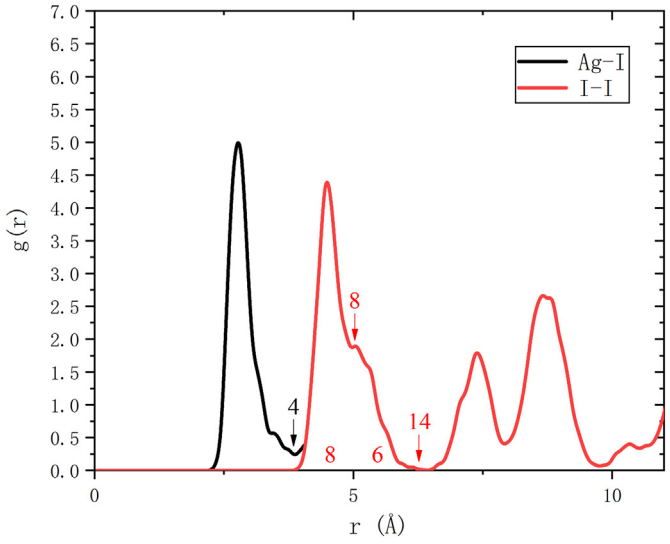

Fig. 12. The RDF at about 600 K obtained by heating the cooled system.

Table 7
The transition temperatures of AgI.

	α → β/γ	β/γ → α
This work	480 K	600 K
RVP	490 K	560 K
Experiment	420 K	

which has been used for ionic diffusion in ionic conductors [31,37,53].

Diffusion in α-AgI is first investigated using the interionic potential listed in Table 1. A neutral system of N = 500 particles (250 Ag^+ and 250 I^-) is considered and the time-step is set to 0.5 fs to ensure the accuracy of the simulation. Ewald summation technique is used to estimate the Coulomb interaction and the cutoff distance is set to 10 Å. The NVT ensemble is initially used for 10^5 MD steps at 773.15 K and then the NPT ensemble is used for another 10^6 MD steps at the same temperature. After equilibration, an additional 10^5 MD steps in NPT ensemble are evolved in the calculation of the MSD curve, as shown in Fig. 7.

Fig. 7 shows that the MSD of I^- is close to zero, suggesting that I^- has negligible diffusion in α-AgI, while the MSD of Ag^+ shows a linearly increasing trend, which implies that Ag^+ has finite diffusion in this system. The diffusion coefficient of Ag^+ is 4.16×10^{-5} $cm^2 \cdot s^{-1}$, which is consistent with experiments [54].

Next, we investigate diffusion of α-AgI at different temperatures to identify the temperature range for which the interionic potential is valid. The system is cooled from 773.15 K to 525.15 K in 25 K or 50 K intervals with 10^5 MD steps in NPT ensemble for each temperature to calculate the MSD curves of Ag^+. The MSD curves are shown in Fig. 8 and then used to calculate the diffusion coefficients. Meanwhile, the MSD of I^- at all temperatures remains close to zero.

The temperature dependence of diffusion coefficients is given by the Arrhenius relation,

$$D = D_0 \exp\left(-\frac{E_A}{RT}\right), \tag{14}$$

where D_0 is the pre-exponential factor, E_A is the activation energy for diffusion, R is the ideal gas constant and T is the temperature. We

derive the linear relationship between $ln(D)$ and $1/T$ from Eq. (14). The diffusion coefficients are calculated from the MSD curve at different temperatures. The relationship between $ln(D)$ and $1/T$ is depicted in Fig. 9, which is in satisfactory agreement with experiments [54]. E_A and D_0 are fitted for both experimental and simulation data. They are listed in Table 6. For comparison, the MD simulation results from the RVP potential are also plotted in Fig. 9 and listed in Table 6.

Fig. 9 and Table 6 show that both the RVP potential and the potential developed in this work are valid to describe the cationic diffusion in α-AgI over a wide range of temperature. All the simulation results are consistent with experiments.

3.4. Phase transition in AgI

Under ambient conditions, the β and γ phase of AgI coexist with each other, with the hexagonal wurtzite ($P\bar{6}_3mc$ [49]) and cubic zinc blende ($F\bar{4}3m$ [55]) crystal structures, respectively. At 420 K, AgI goes through an abrupt first-order phase transition to superionic α phase. Here, we investigate the accuracy of the interionic potential by investigating phase transitions.

MD simulations were performed on the same N = 500 particles α-AgI system at 700 K using the NPT ensemble. When the system is cooled from 700 K to 300 K, at about 480 K, the simulation cell changes to a noncubic shape. The total energy of the system undergoes an abrupt decrease, while the volume of the system experiences a sudden increase simultaneously. This is already indicative of a structural change, as is shown in Fig. 10. The RDF at about 480 K is shown in Fig. 11(a). The nearest neighbor I-I coordination has increased from 8 (α-AgI) to 12 while the nearest neighbor Ag-I coordination remains 4 throughout. This means that the initial α-AgI has transformed to a zinc-blende structure or a wurtzite structure or a combination of them.

Ideally, up to 9.2 Å, the $g_{I\text{-}I}$ should show 6 peaks (12, 18, 20, 38, 50 and 56 neighbors) for hcp iodine sublattice in β-AgI and 4 peaks (12, 18, 42 and 54 neighbors) for fcc iodine sublattice in γ-AgI. From Fig. 11(a), one cannot resolve the situation since the system could either transform to a pure β or γ phase or a mixture of them. The uncertainty is then lifted by analyzing the structure of the transformed system in Fig. 11(b). The fcc and hcp sublattices are made up of close-packed planes of iodine ions that differ only in the stacking sequence of the planes. In fcc, this stacking is along the [111] direction of the conventional unit cell in the sequence ABCABCABC……, as shown in Fig. 11(c), while in hcp it is along the [0001] direction of the hexagonal unit cell in the sequence ABABAB……, as shown in Fig. 11(d). The structure of the transformed system shows a sequence of ABABABCBC, which confirms the mixed nature of the quenched system. Hence, the initial α-AgI transforms to a mixture of β and γ phases at about 480 K.

The cooled system is then heated back to 700 K to study the opposite transition. At about 600 K, the non-cubic simulation cell reverts to a cubic cell representing the initial α-AgI system. The total energy of the system undergoes an abrupt increase, while the volume of the system experiences a sudden decrease simultaneously. The RDF of the system at this temperature is shown in Fig. 12. The nearest neighbor Ag-I coordination is tetrahedral and the first two peaks of $g(r)$ for I-I shows that the first two shells of the iodine lattice contain eight and six particles, which is clearly the characteristic for bcc sublattice. Thus, the mixed system can revert to α phase by heating to about 600 K.

The transition temperatures for α to β/γ phase and β/γ to α phase based on the interionic potential presented in this work and the RVP potential are tabulated in Table 7. The α to β/γ and β/γ to α transition temperatures are determined as 480 K and 600 K in present work, which is in satisfactory agreement with both the RVP potential and experiments. The small errors or the so-called hysteresis phenomenon is common in MD simulations, but the present potential can describe different phases of AgI as a whole.

4. Concluding remarks

In this paper, a new interionic potential for AgI is presented based on the Chen-Möbius lattice inversion and DFT calculations. The accuracy of the potential is checked by comparing MD calculations with experimental data. Simulation results show that the interionic potential developed in this work compared favorably with experiments and *ab initio* calculations in representing several important properties of AgI. Several issues still remain with the interionic potential. The Cauchy relation with pairwise potential, *i.e.*, $C_{12} = C_{44}$ in the cubic system, is one issue. Another issue is to reduce the hysteresis observed in MD simulations in the phase transitions of AgI. These will be addressed in future work.

Acknowledgements

This work was supported by the National Science Foundation (USA) under grant # 1545907, the NSF of China under Grant No. 11304059, the NSF of Heilongjiang Province of China under Grants No. QC2015001, and the International Postdoctoral Exchange Fellowship Program of China under Grants No. 20140016. This research is part of the Blue Waters sustained-petascale computing project, which is supported by the National Science Foundation (awards OCI-0725070 and ACI-1238993) and the state of Illinois. Blue Waters is a joint effort of the University of Illinois at Urbana-Champaign and its National Center for Supercomputing Applications (NCSA).

References

[1] P.G. Bruce, Solid-state chemistry of lithium power sources, Chem. Commun. 19 (1997) 1817–1824.
[2] J.M. Tarascon, M. Armand, Issues and challenges facing rechargeable lithium batteries, Nature 414 (2001) 359–367.
[3] J. Gao, Y. Zhao, S. Shi, H. Li, Lithium-ion transport in inorganic solid state electrolyte, Chin. Phys. B 25 (2016) 018211.
[4] J.W. Fergus, The application of solid fluoride electrolytes in chemical sensors, Sensors Actuators B 42 (1997) 119–130.
[5] N. Imanaka, G. Adachi, Rare earth contribution in solid state electrolytes, especially in the chemical sensor field, J. Alloys Compd. 250 (1997) 492–500.
[6] A. Kumar, K.H. Hsu, K.E. Jacobs, P.M. Ferreira, N.X. Fang, Direct metal nano-imprinting using an embossed solid electrolyte stamp, Nanotechnology 22 (2011) 155302.
[7] K.E. Jacobs, K.H. Hsu, X. Han, A. Kumar, B.P. Azeredo, N.X. Fang, P.M. Ferreira, Solid-state superionic stamping with silver iodide–silver metaphosphate glass, Nanotechnology 22 (2011) 425301.
[8] K.E. Jacobs, P.M. Ferreira, Painting and direct writing of silver nanostructures on phosphate glass with electron beam irradiation, Adv. Funct. Mater. 25 (2015) 5261–5268.
[9] K.E. Jacobs, P.M. Ferreira, Direct e-beam writing of colors on (AgI)x (AgPO3)1 − x glass, J. Vac. Sci. Technol. B 34 (2016) 041605.
[10] C. Tubandt, E. Lorenz, Molekularzustand und elektrisches Leitvermögen kristallisierter Salze, Z. Phys. Chem. 24 (1914) 513–542.
[11] W. Kohlrausch, Das electrische Leitungsvermögen von Chlorsilber, Bromsilber und Jodsilber, Ann. Phys. Chem. 17 (1882) 642–654.
[12] K. Arndt, Leitfähigkeitsmessungen an geschmolzenen Salzen, Z. Elektrochem. 12 (1906) 337–342.
[13] K. Arndt, A. Geßler, Leitfähigkeitsmessungen an geschmolzenen Salzen, Z. Elektrochem. 14 (1908) 662–665.
[14] A. Kvist, A.M. Josefson, The electrical conductivity of solid and molten silver iodide, Z. Naturforsch. 23a (1968) 625–626.
[15] P.C. Allen, D. Lazarus, Effect of pressure on ionic conductivity in rubidium silver iodide and silver iodide, Phys. Rev. B 17 (1978) 1913–1927.
[16] G. Aminoff, Svensk mineralogisk forskning: En återblick, GFF 43 (1921) 188–201.
[17] L.W. Strock, Ergänzung und Berichtigung zu: "Kristallstruktur des Hochtemperatur-Jodsilbers α-AgJ", Z. Phys. Chem. B 31 (1936) 132–136.
[18] S. Hoshino, Crystal structure and phase transition of some metallic halides (IV) on the anomalous structure of α-AgI, J. Phys. Soc. Jpn. 12 (1957) 315–326.
[19] A.F. Wright, B.E.F. Fender, The structure of superionic compounds by powder neutron diffraction. I. Cation distribution in α-AgI, J. Phys. C 10 (1977) 2261–2267.
[20] M.J. Cooper, M. Sakata, The interpretation of neutron powder diffraction measurements on α-AgI, Acta Crystallogr. A 35 (1979) 989–991.
[21] H. Fuess, K. Funke, J. Kalus, Diffuse neutron scattering from β-and α-AgI, Phys. Status Solidi A 32 (1975) 101–107.
[22] J.B. Boyce, T.M. Hayes, W. Stutius, J.C. Mikkelsen, Position and dynamics of Ag ions in superionic AgI using extended X-ray absorption fine structure, Phys. Rev. Lett. 38 (1977) 1362–1365.
[23] J.B. Boyce, T.M. Hayes, J.C. Mikkelsen, Extended-X-ray-absorption-fine-structure

investigation of mobile-ion density in superionic AgI, CuI, CuBr, and CuCl, Phys. Rev. B 23 (1981) 2876–2896.
[24] T.M. Hayes, J.B. Boyce, J.L. Beeby, A structural model for superionic conduction, J. Phys. C 11 (1978) 2931–2937.
[25] A.J. MaJumdar, R. Roy, Experimental Study of the Polymorphism of AgI, J. Phys. Chem. 63 (1959) 1858–1860.
[26] K.H. Lieser, Über einige Untersuchungen am Silberjodid im Hinblick auf die Fehlordnung, Z. Phys. Chem. 5 (1955) 125–153.
[27] B.R. Lawn, The thermal expansion of silver iodide and the cuprous halides, Acta Cryst 17 (1964) 1341–1347.
[28] S. Shi, J. Gao, Y. Liu, Y. Zhao, Q. Wu, W. Ju, C. Ouyang, R. Xiao, Multi-scale computation methods: their applications in lithium-ion battery research and development, Chin. Phys. B 25 (2016) 018212.
[29] W. Schommers, Correlations in the motion of particles in α-AgI: a molecular-dynamics study, Phys. Rev. Lett. 38 (1977) 1536–1539.
[30] A. Fukumoto, A. Ueda, Y. Hiwatari, Molecular dynamics study of ionic motion in α-AgI, Solid State Ionics 3-4 (1981) 115–119.
[31] P. Vashishta, A. Rahman, Ionic motion in α-AgI, Phys. Rev. Lett. 40 (1978) 1337–1340.
[32] M. Parrinello, A. Rahman, P. Vashishta, Structural transitions in superionic conductors, Phys. Rev. Lett. 50 (1983) 1073–1076.
[33] F. Shimojo, M. Kobayashi, Molecular dynamics studies of molten AgI. I. Structure and dynamical properties, J. Phys. Soc. Jpn. 60 (1991) 3725–3735.
[34] S. Ahmad, M.A. Khan, M.A. Wahab, Molecular dynamics study of silver iodide, Mater. Focus 2 (2013) 293–297.
[35] N.X. Chen, Modified Möbius inverse formula and its applications in physics, Phys. Rev. Lett. 64 (1990) 1193–1195.
[36] S. Zhang, N.X. Chen, *Ab initio* interionic potentials for NaCl by multiple lattice inversion, Phys. Rev. B 66 (2002) 064106.
[37] Z. Cui, Y. Sun, Y. Chen, J. Qu, *Semi-ab initio* interionic potential for gadolinia-doped ceria, Solid State Ionics 187 (2011) 8–18.
[38] S. Wang, Z. Fan, R.S. Koster, C. Fang, et al., New *Ab Initio* based pair potential for accurate simulation of phase transitions in ZnO, J. Phys. Chem. C 118 (2014) 11050–11061.
[39] N.X. Chen, X.J. Ge, W.Q. Zhang, F.W. Zhu, Atomistic analysis of the field-ion microscopy image of Fe_3Al, Phys. Rev. B 57 (1998) 14203.
[40] S. Zhang, N.X. Chen, Lattice inversion for interatomic potentials in AlN, GaN and InN, Chem. Phys. 309 (2005) 309–321.
[41] P.P. Ewald, Die Berechnung optischer und elektrostatischer Gitterpotentiale, Ann. Phys. 369 (1921) 253–287.
[42] G. Kresse, J. Furthmüller, Efficiency of ab-initio total energy calculations for metals and semiconductors using a plane-wave basis set, Comput. Mater. Sci. 6 (1996) 15–50.
[43] G. Kresse, D. Joubert, From ultrasoft pseudopotentials to the projector augmented-wave method, Phys. Rev. B 59 (1999) 1758–1775.
[44] G. Kresse, J. Furthmüller, Efficient iterative schemes for *ab initio* total-energy calculations using a plane-wave basis set, Phys. Rev. B 54 (1996) 11169–11186.
[45] J.P. Perdew, K. Burke, M. Ernzerhof, Generalized gradient approximation made simple, Phys. Rev. Lett. 77 (1996) 3865–3868.
[46] P.M. Morse, Diatomic molecules according to the wave mechanics. II. Vibrational levels, Phys. Rev. 34 (1929) 57–64.
[47] D.A. Keen, S. Hull, A powder neutron diffraction study of the pressure-induced phase transitions within silver iodide, J. Phys. Condens. Matter 5 (1993) 23–32.
[48] T.A. Fjeldly, R.C. Hanson, Elastic and piezoelectric constants of silver-iodide: study of a material at the covalent-ionic phase transition, Phys. Rev. B 10 (1974) 3569–3577.
[49] G. Burley, Structure of hexagonal silver iodide, J. Chem. Phys. 38 (1963) 2807–2812.
[50] C.S.G. Cousins, New relations between elastic constants of different orders under central force interactions, J. Phys. C Solid State Phys. 4 (1971) 1117–1123.
[51] A. Einstein, Über die von der molekularkinetischen Theorie der Wärme geforderte Bewegung von in ruhenden Flüssigkeiten suspendierten Teilchen, Ann. Phys. 322 (1905) 549–560.
[52] M. von Smoluchowski, Zur kinetischen Theorie der Brownschen Molekularbewegung und der Suspensionen, Ann. Phys. 326 (1906) 756–780.
[53] H. Inaba, R. Sagawa, H. Hayashi, K. Kawamurab, Molecular dynamics simulation of gadolinia-doped ceria, Solid State Ionics 122 (1999) 95–103.
[54] A. Kvist, R. Tärneberg, Self-diffusion of silver ions in the cubic high temperature modification of silver iodide, Z. Naturforsch. 25a (1970) 257–259.
[55] R.B. Wilsey, XXXI. The crystal structure of the silver halides, Philos. Mag. 42 (1921) 262–263.